

Three mechanisms of hydrogen-induced dislocation pinning in tungsten

Y. Li^{1,2,3}, T.W. Morgan¹, D. Terentyev⁴, S. Ryelandt⁵, A. Favache⁵, S. Wang¹, M. Wirtz⁶, J.P.M. Hoefnagels², J.A.W. van Dommelen², G. De Temmerman⁷, K. Verbeken³ and M.G.D. Geers²

¹*DIFFER-Dutch Institute for Fundamental Energy Research, De Zaale 20, 5612 AJ Eindhoven, The Netherlands*

²*Department of Mechanical Engineering, Eindhoven University of Technology, 5600 MB, Eindhoven, The Netherlands*

³*Department of Materials, Textiles and Chemical Engineering, Ghent University (UGent), Technologiepark 46, B-9052, Ghent, Belgium*

⁴*SCK-CEN, Nuclear Materials Science Institute, Boeretang 200, 2400 Mol, Belgium*

⁵*Institute of Mechanics, Materials and Civil Engineering, UCLouvain, Place Sainte Barbe 2 – L5.02.02, 1348 Louvain-la-Neuve, Belgium*

⁶*Forschungszentrum Jülich GmbH, Institut für Energie- und Klimaforschung, Germany*

⁷*ITER Organization, Route de Vinon sur Verdon, CS 90 046, 13067 St Paul Lez Durance Cedex, France*

E-mail address: Y.Li@diffier.nl

Abstract

The high-flux deuterium plasma impinging a divertor degrades the long-term thermo-mechanical performance of its tungsten plasma-facing components. A prime actor in this is hydrogen embrittlement, a degradation mechanism that involves the interactions between hydrogen and dislocations, the primary carriers of plasticity. Measuring such nanoscale interactions is still very challenging, which limits our understanding. Here, we demonstrate an experimental approach that combines thermal desorption spectroscopy (TDS) and nanoindentation, allowing to investigate the effect of hydrogen on the dislocation mobility in tungsten. Dislocation mobility was found to be reduced after deuterium injection, which is manifested as a ‘pop-in’ in the indentation stress-strain curve, with an average activation stress for dislocation mobility that was more than doubled. All experimental results can be confidently explained, in conjunction with experimental and numerical literature findings, by the simultaneous activation of three mechanisms responsible for dislocation pinning: (i) hydrogen trapping at pre-existing dislocations, (ii) hydrogen-induced vacancies, and (iii) hydrogen-stabilized vacancies, contributing respectively 38%, 52%, and 34% to the extra activation stress. These mechanisms are considered to be essential for the proper understanding and modeling of hydrogen embrittlement in tungsten.

Keywords: hydrogen embrittlement, dislocation mobility, nanoindentation, crystal defects, thermal desorption spectroscopy (TDS)

1. Introduction

Hydrogen degrades the mechanical properties of many metals and alloys [1-12], an effect commonly referred to as hydrogen embrittlement (HE). It is essential to consider this mechanism in evaluating the lifetime performance of structural components, in particular, in a nuclear fusion reactor. Indeed, in ITER, the world's largest fusion experiment, an unprecedented high-flux ($\sim 10^{24} \text{ m}^{-2}\text{s}^{-1}$) of deuterium plasma will strike the tungsten plasma-facing components (PFCs) [13]. The lifetime of PFCs will have a strong influence on the efficiency and economic viability of future fusion power plants, thus motivating ongoing investigations. Progress has been achieved in understanding surface modification of tungsten (e.g. blistering) by hydrogen plasma exposure ([11, 14-22]and references therein) and deuterium retention in tungsten [19, 23-28]. This is largely achieved by probing the microstructural origins (e.g., dislocations) of the macroscopic observations. For example, Guo et al. [22] proposed an edge dislocation nucleation and blistering mechanism based on dedicated transmission electron microscope (TEM) experiments, which reveals an essential role of dislocations on blister formation, while Zibrov et al. [28] studied the influence of defects induced by plastic deformation on deuterium retention by controlling the dislocation density using high-temperature tensile tests. Yet, the link between hydrogen plasma exposure and the evolving mechanical properties of tungsten remains unclear [29]. Building on previous studies, this paper aims to shed light on this aspect using well-designed experiments with up to nanoscale resolutions.

The mechanisms associated with hydrogen embrittlement remain controversial although the phenomenon was first recorded nearly 150 years ago [1]. When limiting our scope to the effect of hydrogen on dislocation mobility, which is a controlling factor

for the brittle-to-ductile transition (e.g. in single-crystal tungsten [30]), several different theories exist. All the prevailing mechanisms build on the concept of the Cottrell atmosphere [31], where hydrogen is trapped at dislocation cores and by the elastic fields of dislocations. On the one hand, the glide of a dislocation distorts the atmosphere and gives rise to a drag force on the dislocation (solute drag), according to numerical simulations [32-34]. On the other hand, such hydrogen atmospheres could also shield the interaction of dislocations with elastic stress centers, making an individual dislocation more, rather than less, mobile, known as hydrogen-enhanced localized plasticity (HELP) [35-37]. In between these two theories is the defectant theory, where hydrogen segregation reduces the formation energy of dislocations, vacancies and grain boundaries [38]. For the case where the dislocation generation rate is enhanced, macroscopic softening is observed [39, 40]. For the case that superabundant vacancies are generated, strong dislocation locking is registered, as was reported for aluminum [41].

This paper investigates if the dislocation mobility in tungsten is reduced or enhanced by hydrogen. Our approach to this problem consists of two novel aspects: (i) tracing and isolating hydrogen trapping at different defects, and (ii) probing the corresponding mechanical behavior at the microscale. For (i), a deuterium flux will be introduced into recrystallized tungsten using a low energy plasma exposure, allowing unambiguous thermal desorption spectroscopy (TDS) afterward. Combined with TMAP7 simulations [42], information on defect types and densities can be obtained. Thereafter, deuterium will be gradually released from the defects by annealing at different temperatures, followed by mechanical testing. To probe the mechanical behavior at the level of single grains, a spherical nanoindentation method is used, from which meaningful indentation

stress-strain data can be extracted [43, 44]. Unlike the widely used Oliver-Pharr method which measures hardness and Young's modulus [45], the adopted method captures the full elastic-plastic response (indentation stress vs. indentation strain) of materials under contact loading, in addition to the high spatial resolution of nanoindentation. As will be shown in this paper, combining these measurements and simulations yields unprecedented insights into the interaction between deuterium and dislocations in tungsten.

2. Experimental and numerical procedure

2.1 Deuterium plasma exposure

Polycrystalline tungsten (PLANSEE[®], 99.97% purity, Ø 20 mm, 1 mm thick) was recrystallized in vacuum at 2000 K for 2 h. The samples were ground and polished using a standard metallographic procedure [46], and then electro-polished in a 0.4 % g/ml aqueous NaOH solution at a DC voltage of 15 V and a current density of ~ 191 A/m². Figure 1(a) shows a secondary electron (SE) micrograph of the recrystallized microstructure with ~ 30 µm grains. Deuterium plasma exposure was carried out using the linear plasma generator Nano-PSI (described in [47]). The full-width half-maximum (Gaussian distribution) of the plasma beam was ~ 40 mm, which is much larger than the analyzed area of ~ 500 µm. Therefore, the samples were considered to be subjected to a uniform plasma exposure. The particle flux was ~3×10²⁰ m⁻²s⁻¹, as measured with a Langmuir probe. The ion energy (originally ~ 0.25 eV) was increased via electrical biasing of the target to 50 eV to increase retention [48]. The sample surface temperature was ~ 325 K and the exposure time was 4000 s. Accordingly, the ion fluence is ~1.2×10²⁴ m⁻².

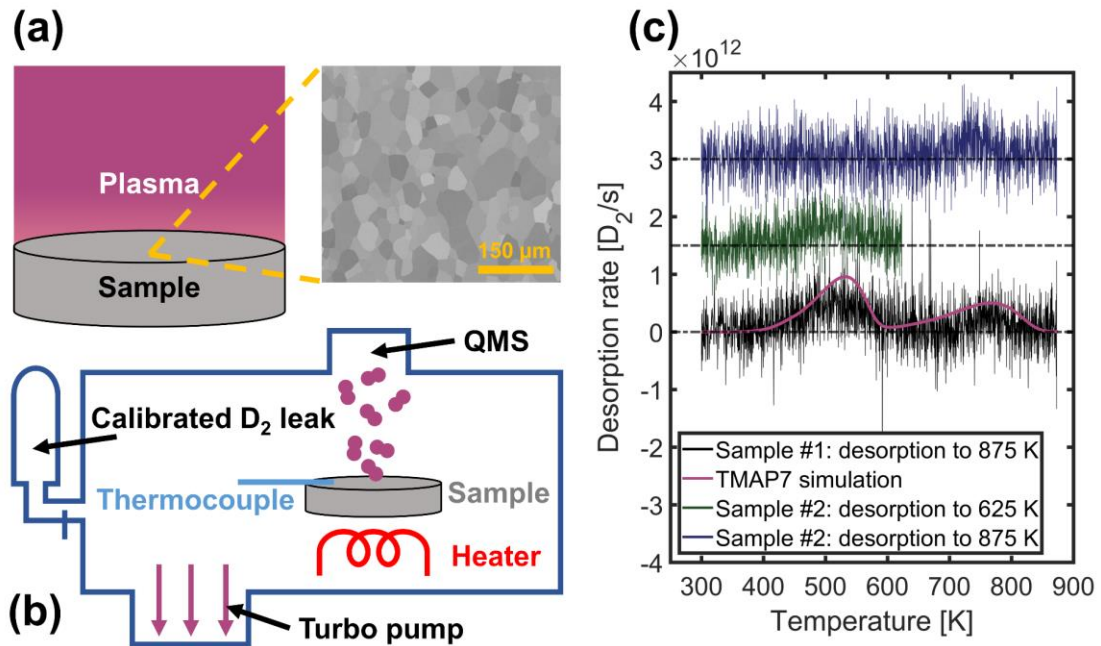


Figure 1. Schematic illustration of the methodology to trace and isolate deuterium trapping at different defects in tungsten with (a) deuterium plasma exposure on a recrystallized tungsten sample. The representative microstructure (SE micrograph) is displayed on the right. (b) Schematic diagram of the thermal desorption spectrum (TDS) set-up. (c) The measured and simulated thermal desorption spectra. Sample #1 was continuously annealed to 875 K (black spectrum). Sample #2 was first annealed to 625 K to desorb the peak around 500 K (green spectrum). After nanoindentation at room temperature, it was annealed to 875 K to release the peak near 750 K (blue spectrum). The two spectra of sample #2 have been shifted up for clarity, as indicated by the dotted background lines. The TMAP 7 simulation details are described in the caption of Table 1. Based on the TMAP 7 analysis, the 1st peak corresponds to deuterium trapping at dislocations and the 2nd peak denotes deuterium trapping at vacancies (color online).

2.2 Thermal desorption spectroscopy and spectrum modeling

Deuterium trapping at defects was studied using TDS, as schematically shown in figure 1(b). An exposed sample placed in a vacuum vessel was heated with a linear temperature ramp (0.5 K/s). At sufficiently high thermal energy, the deuterium atoms release from defects, diffuse to the surface, recombine into molecules, and are registered by a quadrupole mass spectrometer (QMS, Microvision 2, MKS[®]). The base pressure of the TDS chamber is $\sim 10^{-7}$ Pa at room temperature and rises to $\sim 10^{-4}$ Pa at the highest annealing temperature (1173 K). A K-type thermocouple was clamped to the sample surface and was connected to the heater by a feedback control loop. The QMS signal of D₂ molecules was quantified by a calibrated leak bottle with a certified accuracy of less than $\pm 10\%$. During each measurement, the sample was held at the set

temperature (e.g. 625 K) for 5 min to allow for sufficient desorption. In between the nanoindentations, the sample was stored in a desiccator to minimize the negative effects of air exposure [49]. The stepwise TDS and nanoindentation were completed within 4 weeks.

To extract more information from the measured TDS spectrum, the underlying diffusion-trapping process of deuterium transport in tungsten was simulated using TMAP7 [42, 50]. The diffusion coefficient of deuterium in tungsten was taken from [51]. This one-dimensional program also includes recombination of two deuterium atoms at the surface to a D₂ molecule, with a rate coefficient of $3.2 \times 10^{-15} [\text{m}^4 \text{s}^{-1}] \times e^{\frac{-1.16}{k_B T}}$ in this study, as taken from [52]. The dislocation and vacancy distribution were considered to be uniform up to a depth of 10 μm , estimated as $\sqrt{2Dt}$, with an effective diffusion coefficient D ($10^{-14} \text{m}^2 \text{s}^{-1}$) from [53, 54] and the exposure time $t = 4000$ s. The motivation for and influence of this assumption on the obtained defect densities will be discussed in section 3.1. According to [55], the sample was discretized into 64 depth layers, with a varying thickness from 2.5 nm to 100 μm . The simulation time step was 0.5 s.

2.3 Spherical nanoindentation

Nanoindentation was performed on an Agilent G200[®] nanoindenter equipped with continuous stiffness measurement (CSM) [56] using a diamond, conical indenter with a spherical tip with a radius of 12.86 μm (calibrated on fused silica according to [57]). CSM was run at a displacement amplitude of 2 nm and a frequency of 45 Hz. The load rate divided by the current load was set to 0.05 s^{-1} and the maximum displacement into the sample was 350 nm. Thermal drifts were below 0.05 nm/s.

3. Results and discussion

3.1. Thermal desorption spectrum analysis

Figure 1(c) plots the measured and simulated TDS spectra. The black spectrum reveals two peaks, one around 510 K and one around 760 K, consistent with previous studies on deuterium retention in tungsten [58-60]. The trapping density and trapping energy are estimated by matching the TMAP7 simulation to the experimental data. The corresponding results are summarized in Table 1 and are consistent with the literature. The dislocation density is inferred from [61, 62], as measured by transmission electron microscopy (TEM), to be in the range $(1.9 \pm 1.4 - 5.1 \pm 1.7) \times 10^{12} \text{ m/m}^3$ for pure tungsten from the same manufacturer which was recrystallized at 2000 K for 0.5 h and at 1873 K for 1 h. At $\sim 325 \text{ K}$, the hydrogen atom trapped per unit length of dislocation is calculated to be 1 \sim 2 in [63]. The trap density $(\frac{\text{dislocation density} \times \text{hydrogen atom trapped per unit length}}{\text{lattice number density of tungsten}})$ is therefore in the order of 1.0×10^{-6} atomic fraction. The input dislocation detrapping energy lies in the range of atomistic simulations [26, 63], 1.28-1.36 eV for an edge dislocation, and 0.92-0.96 eV for a screw dislocation. The vacancy detrapping energy agrees well with atomistic simulations [64-66], being 1.65-2 eV up to the second filling level. Note that the detrapping energy is the sum of H binding energy to a type of defect and the activation energy of H diffusion in W, which is well accepted to be 0.39 eV [51]. The simulated spectrum has been down-scaled by a factor of ~ 2 to match the measured spectrum. This scaling factor accounts for the fact that a portion of deuterium (D) atoms desorbs as HD and D₂O, as well as for the uncertainty on the exact value of the dislocation density.

Table 1. Input for the TMAP7 simulation that resulted in an optimal match for the TDS spectrum in figure 1(c).

Trapping type	Trapping density [at.fr]	Detrapping energy [eV]	Trapping depth [μm]
Dislocation	4.0×10^{-6}	1.25	10
Vacancy	2.8×10^{-6}	1.85	

The influence of the assumed defect distribution on the TMAP7 modeling results is assessed here. First, in the above analysis, the trapping depth is estimated using the diffusion length ($\sqrt{2Dt}$) with an effective diffusion coefficient D ($10^{-14} \text{ m}^2\text{s}^{-1}$) taken from [53, 54], which was measured near room temperature. The measured effective diffusion is equivalent to a combination of ideal Frauenfelder diffusivity and trapping at defects, as considered in TMAP7. Using this effective diffusion coefficient therefore gives a reasonable estimate of the trapping depth in the TMAP7 simulation. Second, both dislocations and vacancies are assumed to be uniformly distributed. For the dislocations, this is straightforward, as the sample was annealed above the recrystallization temperature for 2 hours. For the vacancies, this is justified by their formation mechanism, as discussed in the next paragraph. The uniform distribution assumption is supported by the nuclear reaction analysis (NRA) measurements from [62]. Under similar plasma conditions (ion energy, particle flux, and surface temperature) and tungsten grade (recrystallized), the deuterium concentration profile is shown to be uniform up to 7 μm . Note that 7 μm is the maximum probing depth of most current NRA machines. Beyond 7 μm and extending to a reasonable distance, for example, 10 μm , as assumed in this study, the uniform distribution assumption is expected to remain valid. If there would have been a deuterium concentration gradient due to a nonuniform vacancy distribution, it would have appeared in the very first few micrometers, as frequently reported in the literature. Furthermore, we have calculated

another extreme case, where we considered a diffusion length (40 μm) using the ideal Frauenfelder diffusion coefficient [51]. We found that the defect density reduced by a factor of 4 and the detrapping energy decreased 0.1 eV for both types of defects. This suggests that the defect distribution assumption made here has a minor effect on the TMAP7 modeling results and therefore the conclusions made are considered to be valid. The TMAP7 modeling results suggest the formation of vacancies during plasma exposure. As shown in Table 1, the TMAP7 input vacancy density (to match the measured spectrum) is significantly higher than the thermal equilibrium vacancy concentration of tungsten. As extrapolated from [67], the atomic fraction of thermal equilibrium vacancy in tungsten is 5.78×10^{-9} at 2000 K and 2.53×10^{-61} at 300 K. A conservative estimation, taking the thermal vacancy concentration at 2000 K (the recrystallization temperature used) and assuming that the sample was quenched from that temperature preventing vacancy annihilation, would suggest that the actual vacancy concentration is a few hundred times higher than the thermal vacancy concentration (2.8×10^{-6} vs. 5.78×10^{-9}). A reasonable explanation is that vacancies were created in the tungsten bulk during deuterium plasma exposure. Note that the implantation depth of 50 eV deuterium plasma in tungsten is only 2.86 nm [68]. The observed superabundant vacancy formation agrees with the defectant theory, established by statistical thermodynamics [38]. A more recent first-principle study reveals that hydrogen trapping at a screw dislocation in tungsten can spontaneously punch out a vacancy jog [26, 69]. This is consistent with the fact that the TMAP7 input dislocation density and vacancy density are of the same order of magnitude, which is not surprising if vacancies nucleate on pre-existing dislocations. This also justifies the assumption that vacancies are uniformly distributed since they nucleate on pre-existing dislocations and the dislocation distribution is uniform. The vacancy formation

mechanism is controlled by temperature, which determines the number of deuterium atoms a dislocation loop can trap and, therefore, the subsequent spontaneous generation of vacancy jogs [26, 63]. Since the temperature difference across the top 10 μm is negligible during plasma exposure (because of the low heat flux), the vacancy formation kinetics are similar and therefore its distribution profile after plasma exposure should be uniform. Using a similar vacancy formation mechanism, Fukai et al. have explained why *bulk* superabundant vacancies are formed to much higher depths beneath the surface in various metals under high hydrogen pressures [70, 71]. To summarize, the results suggest that (i) deuterium loading facilitates vacancy formation, with vacancies nucleating on pre-existing dislocations, and (ii) deuterium atoms are being trapped at pre-existing dislocations and the deuterium-induced vacancies after plasma exposure.

3.2. Mechanical testing by nanoindentation

The extraction of the indentation stress-strain response using a spherical nanoindentation method is demonstrated below. Pioneered by Kalidindi's group [43], this method is essentially a two-step process, as illustrated in figure 2. The first step is to accurately establish the effective initial contact point by translating the raw load-displacement ($P - h$) data [72] such that the initial elastic loading segment lines up with the predictions of Hertz's theory for a spherical body contacting a half-plane [73]. The second step, figure 2(b), is to introduce the indentation stress and strain measures to convert the corrected $P - h$ response into an indentation stress-strain curve (see Ref. [43] for more details). The obtained indentation stress-strain curves from multiple grain interiors on the reference sample were found to be *continuous* and similar, as displayed in figure 2(c), which are consistent with previous studies on recrystallized tungsten [43,

74]. It should be noted that the stress measure we use here is called indentation stress, which is different from the yield stress used in a uniaxial tensile/compression test. Approximately, the indentation stress can be converted into yield stress by dividing it by a factor of ~ 2.2 , as demonstrated with finite element analysis [75]. In this way, the yield stress of our reference sample is roughly 1.8 GPa (Fig. 2c), which is close to micropillar compression measurements on tungsten [76]. The nanoindentation measurements are therefore realistic. It is important to point out that there are no pop-ins (strain bursts) before plasma exposure. This distinguishes this study from previous work [77-79] which uses a sharp Berkovich tip. The corresponding differences and implications will be discussed in section 3.3.

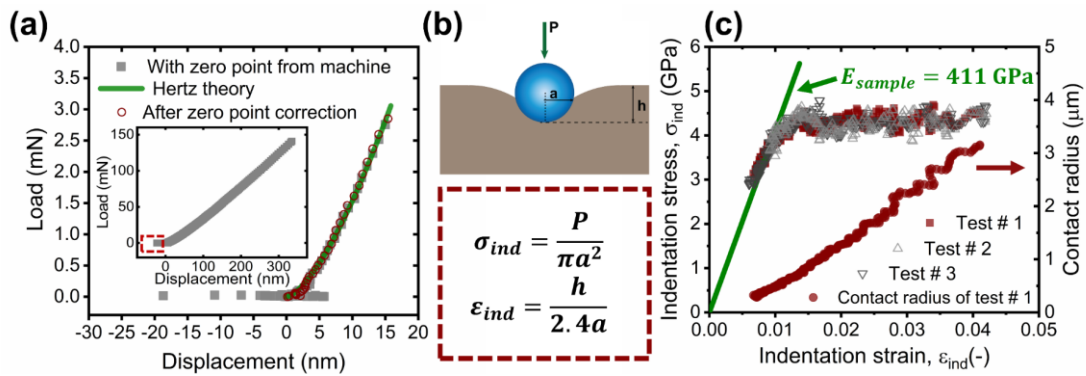


Figure 2. Extraction of the indentation stress-strain curve using the spherical nanoindentation method [43] on a reference recrystallized tungsten sample. (a) Identification of the effective initial contact point using Hertz’s theory. The machine identifies the point of initial contact (zero point) when the stiffness signal (measured by CSM) first reaches 200 N/m. As a consequence, the initial elastic loading segment of the raw data set exhibits some scattering and deviates from Hertz’s theory, which is also highlighted in the inset where the raw data up to the end of the loading segment is displayed. (b) Schematic representation of nanoindentation and the introduced stress (σ_{ind}) and strain (ϵ_{ind}) measures. (c) Three indentation stress-strain curves from three different grain interiors where the indentation stress and strain have been calculated using the equations in (b). The contact radius (a in the middle schematic drawing) for test #1 is also shown on the right axis. a is calculated from stiffness (measured by CSM), see Ref. [43] for more details. Due to the noise in the initial stiffness signal, a portion of the initial stress-strain curve is missing (color online).

3.3. Stepwise TDS and nanoindentation

Stepwise TDS and spherical nanoindentation at room temperature were combined to link the microstructure and mechanical response. One such example is displayed in figure 3. A sample with an ‘identical’ microstructure as the previous one (Sample #1 in

figure 1(c)) was first characterized by nanoindentation after the same plasma exposure. The same sample was then annealed to 625 K to desorb the deuterium trapped at pre-existing dislocations (with a detrapping energy of 1.25 eV, see Table 1), before subsequent nanoindentation. Thereafter, the same sample was annealed to 875 K to release the trapped deuterium at deuterium-induced vacancies (with a detrapping energy of 1.85 eV), followed again by nanoindentation. Finally, the same sample was annealed at 1173 K for 2 hours, and measured by nanoindentation one more time. In each case, the nanoindentation was carried out on the same grain, with sufficient spacing (at least 10 μm) to create independent indentation measurements. The corresponding stepwise TDS spectra of this sample are shown in figure 1(c). A distinctive feature of the obtained indentation stress-strain curves after plasma exposure is the emergence of pop-ins. The indentation pop-in stress (σ_{pop-in} defined in figure 3) gradually drops with the two intermediate annealing stages but recovers in the last annealing stage. A similar trend in terms of the indentation strain burst ($\Delta\varepsilon_{pop-in}$ defined in figure 3) is also observed. Another important observation is that only after plasma exposure and before TDS annealing, the indentation stress-strain curves display some strain hardening (H_{ind}). The above phenomena hold for the measured 10 grains in an average sense, as summarized in figure 4. The raw data from 10 grains are provided in Appendix A as well. The average indentation pop-in stresses for the four stages are 9.18 ± 1.14 , 7.63 ± 1.03 , 6.24 ± 0.60 , and 6.89 ± 0.75 GPa, respectively. In contrast, the indentation yield stress before the exposure is 4.10 ± 0.16 GPa.

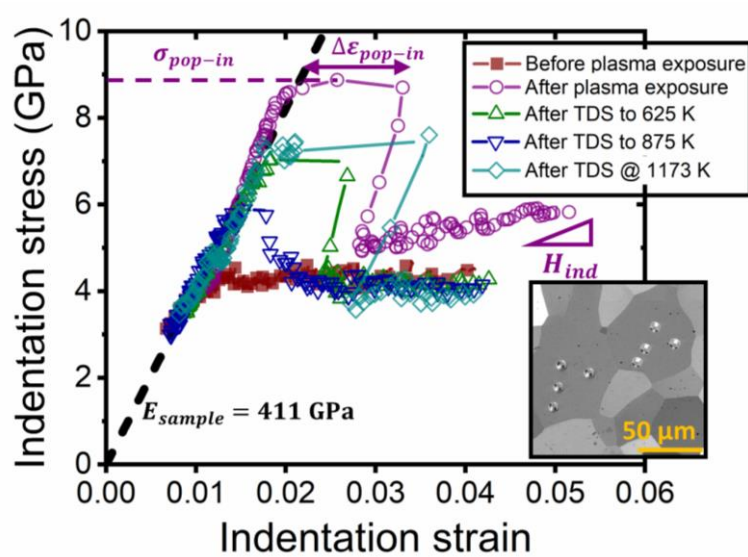


Figure 3. Indentation stress-strain response of the plasma exposed sample with different annealing stages. The nanoindentation was performed at room temperature after each specified TDS measurement. TDS @ 1173 K has the same heating rate (0.5 K/s) as the previous annealing stages but with an extra holding time of 2 hours. The indentation stress-strain curve before the exposure is from another reference sample, as previously displayed in figure 2(c). The rest of the 4 indentation measurements are from the same grain interior, shown in the inset BSE SEM image. The definition of σ_{pop-in} , $\Delta\epsilon_{pop-in}$, and H_{ind} are schematically illustrated. H_{ind} is obtained by linear regression of the indentation strain values in the range of a strain offset of 0.025 and 0.035. This definition is used for comparison purposes only. Note that only half of the data points are shown to improve the clarity of the figure but without affecting the results.

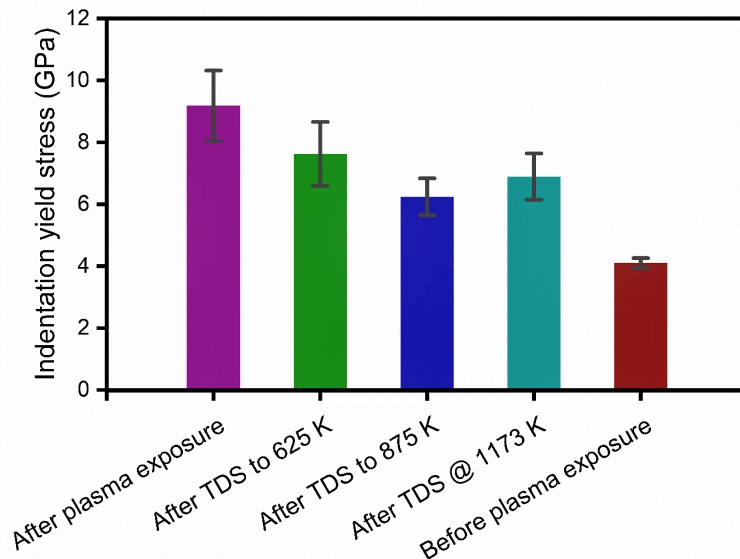


Figure 4. Averaged indentation yield stress (equivalent to σ_{pop-in}) for the 10 grains in the different stages.

The observed 4-stage pinning process is rationalized as follows. First, in figure 5(a), some relevant length scales are analyzed to rule out other potential origins of pop-ins.

According to Hertz's theory [73], the maximum resolved shear stress occurs at a depth of $0.48 a$, which corresponds to $\sim 0.5 \mu\text{m}$ in this study, based on the measured contact radius a just before the pop-in. The primary indentation zone (width \times depth) at the end of loading, estimated as $2a \times 2.4a$ [43], is indicated by the green box. The implantation depth of a 50 eV deuterium plasma on tungsten is $\sim 3 \text{ nm}$ [68]. Therefore, the pop-ins cannot be caused by (dislocations or vacancies created by) plasma implantation. On the other hand, the deuterium diffusion length was $\sim 10 \mu\text{m}$, resulting in a nearly uniform microstructure within the range of the indentation stress field. Therefore the pop-ins cannot have originated from the 'hard-film-on-soft-substrate' effect [80]. Moreover, by deliberately using a relatively large tip with a radius of $12.86 \mu\text{m}$ and selecting indentation spots away from the grain boundaries, pop-ins due to dislocation source starvation [81-87] or grain boundaries [88-90] were avoided. Therefore the observed pop-ins should be interpreted as caused by the activation of slip of pre-existing dislocations that are pinned by the microstructure originating from deuterium exposure. Figure 5(b)-(e) schematically sketches the 4 stages of this dislocation pinning. After plasma exposure, the strongest pinning is imposed by deuterium segregation to pre-existing dislocations and deuterium filled vacancies. By releasing the trapped deuterium atoms from pre-existing dislocations, the activation stress for dislocation mobility drops. Subsequent desorption of the trapped deuterium atoms at vacancies further reduces the activation stress. However, vacancy coalescence in the final annealing stage increases the pop-in stress. The above analysis is supported by the solute drag theory [32], the locking of dislocations by vacancies [41], atomistic calculations showing stabilization of vacancies by deuterium [71, 91, 92], and observation of vacancy coalescence [93], respectively.

In further support of the consistency of the proposed mechanism, we note that apparent strain hardening was only observed after plasma exposure, where deuterium atoms were trapped at pre-existing dislocations. For deuterium, if its diffusion mobility is of the same order as the dislocation mobility, it could give rise to hardening [40, 94, 95]. The diffusion speed v_{diff} can be estimated as [96]: $v_{diff} = \frac{2D}{\lambda} \approx 0.4$ (0.28) mm/s, where D (6.63×10^{-14} m²/s) is the diffusion coefficient of hydrogen (or deuterium by down-scaling a factor of $\sqrt{2}$ [92], yielding 0.28 mm/s) in tungsten at room temperature [51] and λ (3.16×10^{-10} m) is the lattice constant of tungsten [97]. Here, for the deuterium atoms to catch up with the gliding dislocations driven by the externally applied stress, their diffusion speed is determined by the migration barrier between adjacent tetrahedral sites in tungsten. Therefore, it is appropriate to use the extrapolated ideal Frauenfelder diffusion coefficient [51] rather than the effective diffusion coefficient [53, 54]. The dislocation mobility v_{dis} is estimated using Orowan's equation [98] as: $v_{dis} = \frac{\dot{\epsilon}}{b\rho_M} \approx 0.3$ mm/s, where $\dot{\epsilon}$ (0.009 s⁻¹) is the measured indentation strain rate, b (0.274×10^{-9} m) is the Burgers vector, and ρ_M (10^{11} m⁻²) is the mobile dislocation density. Note that ρ_M is typically at least 10 times smaller than the immobile dislocation density [99], therefore, 10^{11} m⁻² is used in the above calculation compared to 10^{12} m⁻² in the TMAP7 simulation. The results support the proposed picture. Based on the analyses above and the measurements summarized in figure 4, the indentation pinning stresses exerted by deuterium trapping at pre-existing dislocations, deuterium-induced vacancies, and deuterium-stabilized vacancies are 1.55, 2.14, and 1.39 GPa, correspond to an extra activation stress for dislocation mobility of respectively 38%, 52%, and 34%. Note that although the indentation stress is used, the obtained results after normalization, that is increase in percentage, are independent of this specific choice of stress measure.

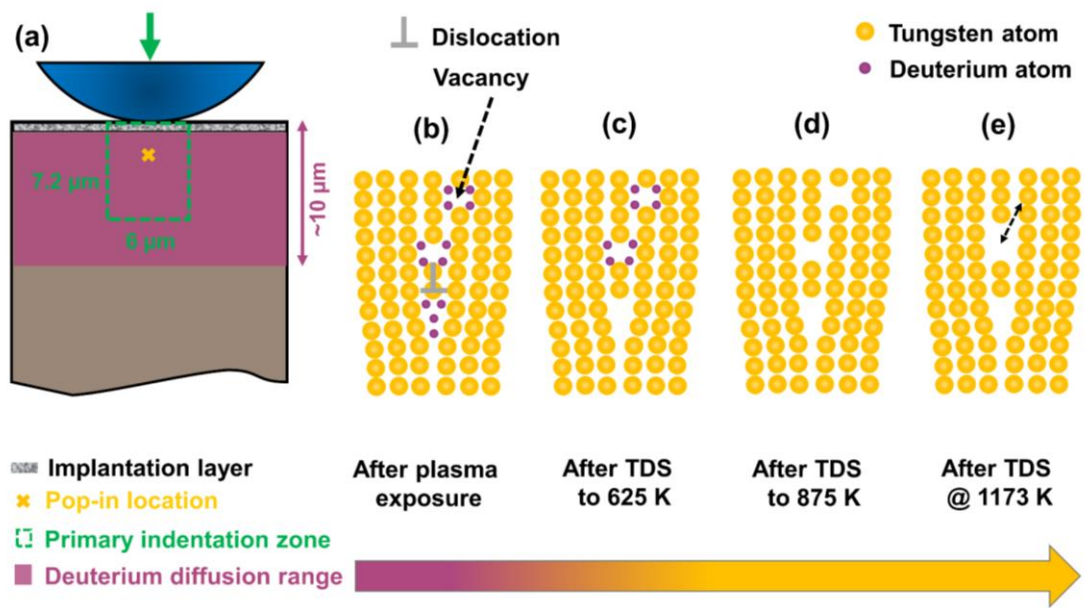


Figure 5. Sketch of the dislocation pinning mechanisms (not to scale). (a) The relevant length scales. The deuterium plasma implantation layer is ~ 2.86 nm [68]. The maximum resolved shear stress at a pop-in event occurs at a depth of ~ 0.5 μm [73]. The primary indentation zone (width \times depth) at the end of the loading is ~ 6 $\mu\text{m} \times 7.2$ μm [43]. The deuterium diffusion range is ~ 10 μm . (b) After deuterium plasma exposure, deuterium atoms are trapped at pre-existing dislocations (simplified as an edge dislocation represented by the extra tungsten atom column) and deuterium-induced vacancies (represented by a missing tungsten atom in the lattice). (c) TDS to 625 K releases deuterium atoms from pre-existing dislocations. (d) TDS to 875 K desorbs trapped deuterium atoms at deuterium-induced vacancies. (e) Vacancies coalescence when annealing at 1173 K for 2 hours. In principle, some vacancy clusters may have formed in the early TDS annealing stages but this is a minor effect and therefore not considered here for simplicity. (color online).

In the above analysis, we implicitly assumed that the dislocation and vacancy structures are not significantly modified by the stepwise TDS annealing, which is justified as follows. For dislocations, since the sample has been recrystallized at 2000 K for 2 hours, it is appropriate to assume that a stabilized dislocation structure has been formed during such a heat treatment, which subsequently remains stable. This hypothesis is supported by the stepwise TDS and nanoindentation measurements in Fig.3, where after pop-ins, the stress-strain curves are highly similar. This would not be the case if some dislocations were annealed during the TDS measurement. The vacancy evolution analysis is based on recent work by Zibrov et al. [93]. These authors traced the vacancy annealing kinetics using positron annihilation analyses and found that vacancies start to coalescence near 500 K and begin to annihilate near 1200 K. Vacancy coalescence

has been shown to give rise to a higher pinning stress (Fig. 3). If it would dominate in the first two TDS annealing stages (TDS to 625 K and 875 K, respectively), it would have resulted in continuously growing pop-in stresses rather than the opposite trend as observed in Fig. 3. It is therefore justified to conclude that the varying pop-in stresses in the first two TDS annealing stages are dominated by deuterium de-trapping from the defects. Moreover, considering that the vacancy concentration in the samples of [93] should be considerably higher than the one considered here since it results from 200 keV H ions, the vacancy coalescence and annihilation temperatures in our sample would shift to higher temperatures. In this way, vacancy coalescence can be expected to play an even minor role while reaching our original conclusions. Overall, the dislocation and vacancy structures are not expected to be significantly modified by the first two TDS annealing stages.

The effect of native surface oxidation on the obtained nanoindentation results is also expected to be negligible. According to [100], tungsten has a ~10 nm native surface oxide layer. This could be troublesome for studies using a sharp Berkovich tip, where the tip radius is also a few tens of nanometers. However, this is not a problem in the present study. First, here a micrometer size tip with a radius of 12.86 μm is used, which is significantly larger than the oxide layer. Second, using the procedure outlined in [43], the measured load-displacement curve, Fig. 2a, has been rigorously corrected to make sure that the measured raw data is not influenced by the oxide layer. Third, the pop-ins occur at an indentation depth of approximately 500 nm below the surface (see the length scale analysis in Fig. 5a). The oxide layer therefore is not expected to affect the obtained results. The same analysis applies to surface roughness (after electro-polishing) and possible atomic layer impurity depositions during plasma exposure.

It is worth mentioning that the pop-ins observed here are distinct from those described in [77-79]. In those studies, the effect of hydrogen plasma exposure on the pop-in response in tungsten was investigated, whereby it was concluded that the hydrogen plasma exposure reduces the pop-in probability. In their work, a sharp Berkovich tip was used and pop-ins already occurred before plasma exposure, which is due to dislocation source starvation [81, 83, 101, 102]. In our study, a large spherical tip (12.86 μm) was deliberately chosen to be outside of the dislocation starvation regime [101], through which pop-ins only appeared after plasma exposure. Therefore, our results probe a new regime that is complementary to previous related studies.

4. Conclusion

In summary, the obtained experimental results based on the combination of TDS and spherical indentation measurements accompanied by the computational as well as literature analysis suggest the existence of three types of deuterium-induced dislocation pinning phenomena in tungsten, which are linked to three underlying mechanisms: (i) deuterium segregation at pre-existing dislocations; (ii) formation of deuterium-induced vacancies; and (iii) formation of deuterium-stabilized vacancies. Although there are no direct atomistic observations as yet, the proposed mechanisms are self-consistent and are supported by multiple experimental and simulation studies.

This study reveals highly relevant new details of the interaction between deuterium and dislocations in tungsten. The observed strain hardening agrees with previous studies [78, 95, 103] on tungsten. Moreover, we were also able to capture the pinning effect by deuterium-induced vacancies, which has only been experimentally reported for aluminum as measured with an environmental transmission electron microscope [41]. Furthermore, for the first time, we experimentally identified that a deuterium-vacancy

complex requires a higher activation stress for dislocation mobility than an empty vacancy (or vacancy cluster) (Fig. 5(c) to (d)). These details are expected to be essential for a proper understanding and modeling of hydrogen embrittlement in tungsten. For example, this study implies that the presence of hydrogen makes tungsten brittle by reducing dislocation mobility. This could lead to accelerated structural failure of the plasma-facing components under fusion-relevant plasma loadings [104] and should be examined in greater detail.

We would like to point out that in this study, recrystallized tungsten is used to simplify the investigated system, for example, to have a good knowledge of the microstructure before plasma exposure and to keep it stable during TDS measurements. In this way, a clear conclusion can be drawn from the experiments. The conclusion itself, however, i.e. hydrogen-induced reduced dislocation mobility, can be applied to any tungsten grade. For the mechanical behavior of tungsten, dislocation mobility is undoubtedly one of the most important parameters. Therefore, the reported results here are expected to be relevant when developing plasma-facing materials and components for fusion devices.

As a final remark, we are confident that the methodology demonstrated here can also be applied to other material systems.

Acknowledgments

DIFFER is part of the institutes organisation of NWO. This work was supported by the European Commission and carried out within the framework of the Erasmus Mundus International Doctoral College in Fusion Science and Engineering (FUSION-DC). This work has been carried out within the framework of the EUROfusion Consortium and

has received funding from the Euratom research and training programme 2019-2020 under grant agreement No 633053. The views and opinions expressed herein do not necessarily reflect those of the European Commission or the ITER organization.

Appendix A. Summary of the indentation measurements

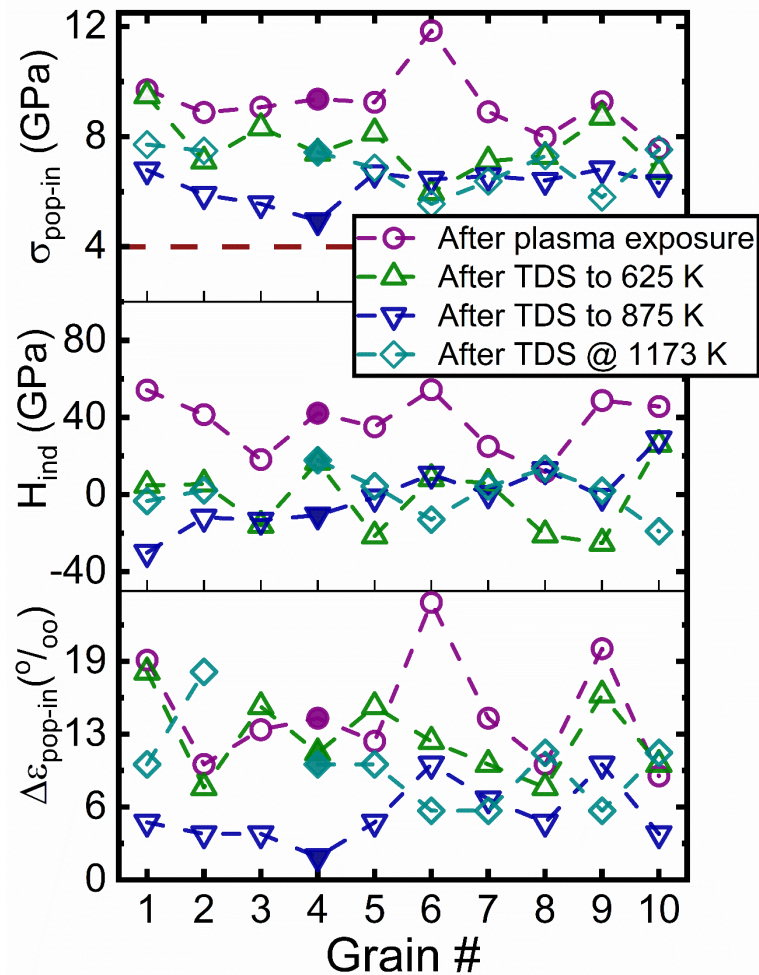


Figure A. σ_{pop-in} , H_{ind} , and $\Delta\epsilon_{pop-in}$ from 10 grains in the 4 stages, respectively. Lines are shown only as a visual guide. The red dashed line in the top panel denotes the indentation yield stress before exposure, identified through a 0.2% indentation strain offset. Grain #4 (filled symbols) corresponds to the results shown in figure 3.

References

- [1]Johnson W. H. 1875 *Proc. R. Soc. London* **23** 168
- [2]Novak P., Yuan R., Somerday B. P., Sofronis P. and Ritchie R. O. 2010 *J. Mech. Phys. Solids* **58** 206
- [3]Song J. and Curtin W. A. 2011 *Acta Mater.* **59** 1557
- [4]Martin M. L., Sofronis P., Robertson I. M., Awane T. and Murakami Y. 2013 *Int. J. Fatigue* **57** 28
- [5]Depover T., Wallaert E. and Verbeken K. 2016 *Mater. Sci. Eng. A* **649** 201

- [6]Hajilou T., Deng Y., Rogne B. R., Kheradmand N. and Barnoush A. 2017 *Scr. Mater.* **132** 17
- [7]Ogawa Y., Birenis D., Matsunaga H., Thøgersen A., Prytz Ø., Takakuwa O. and Yamabe J. 2017 *Scr. Mater.* **140** 13
- [8]Zhang Z., Obasi G., Morana R. and Preuss M. 2016 *Acta Mater.* **113** 272
- [9]Tarzimoghadam Z., Ponge D., Klöwer J. and Raabe D. 2017 *Acta Mater.* **128** 365
- [10]Xie D.-G., Wang Z.-J., Sun J., Li J., Ma E. and Shan Z.-W. 2015 *Nat. Mater.* **14** 899
- [11]Jia Y. Z., Liu W., Xu B., Qu S. L., Shi L. Q. and Morgan T. W. 2017 *Nucl. Fusion* **57** 034003
- [12]van Eden G. G., Morgan T. W., van der Meiden H. J., Matejicek J., Chraska T., Wirtz M. and De Temmerman G. 2014 *Nucl. Fusion* **54** 123010
- [13]Pitts R. A. *et al* 2019 *Nucl. Mater. Energy* 100696
- [14]Ye M. Y., Kanehara H., Fukuta S., Ohno N. and Takamura S. 2003 *J. Nucl. Mater.* **313–316** 72
- [15]Luo G. N., Shu W. M. and Nishi M. 2005 *J. Nucl. Mater.* **347** 111
- [16]Shu W. M., Wakai E. and Yamanishi T. 2007 *Nucl. Fusion* **47** 201
- [17]Lindig S., Balden M., Kh Alimov V., Yamanishi T., Shu W. M. and Roth J. 2009 *Phys. Scr.* **T138** 014040
- [18]Lindig S., Balden M., Alimov V. K., Manhard A., Höschen C., Höschen T., Tyburska-Püschel B. and Roth J. 2011 *Phys. Scr.* **T145** 014039
- [19]Manhard A., Schmid K., Balden M. and Jacob W. 2011 *J. Nucl. Mater.* **415** S632
- [20]t Hoen M. H. J., Balden M., Manhard A., Mayer M., Elgeti S., Kleyn A. W. and Zeijlmans van Emmichoven P. A. 2014 *Nucl. Fusion* **54** 083014
- [21]Jia Y. Z., De Temmerman G., Luo G. N., Xu H. Y., Li C., Fu B. Q. and Liu W. 2015 *J. Nucl. Mater.* **457** 213
- [22]Guo W., Ge L., Yuan Y., Cheng L., Wang S., Zhang X. and Lu G.-H. 2018 *Nucl. Fusion* **59**
- [23]Alimov V. K. and Roth J. 2007 *Phys. Scr.* **T128** 6
- [24]Alimov V. K., Tyburska-Püschel B., Lindig S., Hatano Y., Balden M., Roth J., Isobe K., Matsuyama M. and Yamanishi T. 2012 *J. Nucl. Mater.* **420** 519
- [25]Poon M., Haasz A. A. and Davis J. W. 2008 *J. Nucl. Mater.* **374** 390
- [26]Terentyev D., Dubinko V., Bakaev A., Zayachuk Y., Van Renterghem W. and Grigorev P. 2014 *Nucl. Fusion* **54** 042004
- [27]Zibrov M., Balden M., Morgan T. W. and Mayer M. 2017 *Nucl. Fusion* **57** 046004
- [28]Zibrov M., Balden M., Dickmann M., Dubinko A., Egger W., Mayer M., Terentyev D. and Wirtz M. 2019 *Nucl. Fusion* **59** 106056
- [29]De Temmerman G., Hirai T. and Pitts R. A. 2018 *Plasma Phys. Control. Fusion* **60** 044018
- [30]Gumbsch P., Riedle J., Hartmaier A. and Fischmeister H. F. 1998 *Science* **282** 1293
- [31]Cottrell A. H. and Bilby B. A. 1949 *Proc. Phys. Soc. London, Sect. A* **62** 49
- [32]Cottrell A. H. and Jaswon M. 1949 *Proc. R. Soc. London, Ser. A* **199** 104
- [33]Song J. and Curtin W. A. 2014 *Acta Mater.* **68** 61
- [34]Sills R. B. and Cai W. 2016 *Philos. Mag.* **96** 895
- [35]Birnbaum H. K. and Sofronis P. 1994 *Mater. Sci. Eng. A* **176** 191
- [36]Sofronis P. and Birnbaum H. K. 1995 *J. Mech. Phys. Solids* **43** 49
- [37]Ferreira P., Robertson I. and Birnbaum H. 1998 *Acta Mater.* **46** 1749
- [38]Kirchheim R. 2007 *Acta Mater.* **55** 5129
- [39]Barnoush A., Kheradmand N. and Hajilou T. 2015 *Scr. Mater.* **108** 76

- [40]Kirchheim R. 2012 *Scr. Mater.* **67** 767
- [41]Xie D., Li S., Li M., Wang Z., Gumbsch P., Sun J., Ma E., Li J. and Shan Z. 2016 *Nat Commun* **7** 13341
- [42]Longhurst G. "TMAP7 User Manual, INEEL/EXT-04-02352" 2004.
- [43]Kalidindi S. R. and Pathak S. 2008 *Acta Mater.* **56** 3523
- [44]Pathak S. and Kalidindi S. R. 2015 *Mater. Sci. Eng. R Rep.* **91** 1
- [45]Oliver W. C. and Pharr G. M. 1992 *J. Mater. Res.* **7** 1564
- [46]Vander Voort G. F. *Metallography, principles and practice*: ASM international, 1999
- [47]Ou W., Al R. S., Vernimmen J. W. M., Brons S., Rindt P. and Morgan T. W. 2020 *Nucl. Fusion* **60** 026008
- [48]t Hoen M. H., Mayer M., Kleyn A. W. and Zeijlmans van Emmichoven P. A. 2013 *Phys. Rev. Lett.* **111** 225001
- [49]Moshkunov K. A., Schmid K., Mayer M., Kurnaev V. A. and Gasparyan Y. M. 2010 *J. Nucl. Mater.* **404** 174
- [50]Schmid K. 2016 *Phys. Scr.* **T167** 014025
- [51]Frauenfelder R. 1969 *J. Vac. Sci. Techno.* **6** 388
- [52]Anderl R., Holland D., Longhurst G., Pawelko R., Trybus C. and Sellers C. 1992 *Fusion Technology* **21** 745
- [53]Ikeda T., Otsuka T. and Tanabe T. 2011 *J. Nucl. Mater.* **415** S684
- [54]Ikeda T., Otsuka T. and Tanabe T. 2011 *Fusion Science and Technology* **60** 1463
- [55]t Hoen M. H. J., Mayer M., Kleyn A. W., Schut H. and Zeijlmans van Emmichoven P. A. 2013 *Nucl. Fusion* **53** 043003
- [56]Pharr G. M., Strader J. H. and Oliver W. C. 2011 *J. Mater. Res.* **24** 653
- [57]Weaver J. S., Pathak S., Reichardt A., Vo H. T., Maloy S. A., Hosemann P. and Mara N. A. 2017 *J. Nucl. Mater.* **493** 368
- [58]Manhard A., Schmid K., Balden M. and Jacob W. 2011 *J. Nucl. Mater.* **415** S632
- [59]Ogorodnikova O. V., Roth J. and Mayer M. 2008 *J. Nucl. Mater.* **373** 254
- [60]Terentyev D., De Temmerman G., Minov B., Zayachuk Y., Lambrinou K., Morgan T. W., Dubinko A., Bystrov K. and Van Oost G. 2015 *Nucl. Fusion* **55** 013007
- [61]Manhard A., Balden M. and Elgeti S. 2015 *Pract. Metallogr.* **52** 437
- [62]Mikhail Z., Martin B., Marcel D., Andrii D., Werner E., Matej M., Dmitry T. and Marius W. 2019 *Nucl. Fusion*
- [63]Backer A. D., Mason D. R., Domain C., Nguyen-Manh D., Marinica M. C., Ventelon L., Becquart C. S. and Dudarev S. L. 2018 *Nucl. Fusion* **58** 016006
- [64]You Y.-W.. *et al* 2013 *AIP Advances* **3** 012118
- [65]Heinola K., Ahlgren T., Nordlund K. and Keinonen J. 2010 *Phys. Rev. B* **82**
- [66]Fernandez N., Ferro Y. and Kato D. 2015 *Acta Mater.* **94** 307
- [67]Rasch K. D., Siegel R. W. and Schultz H. 1980 *Philos. Mag A* **41** 91
- [68]Eckstein W. "Calculated Sputtering, Reflection and Range Values (IPP 9/132)" 2002.
- [69]Dubinko V. I., Grigorev P., Bakaev A., Terentyev D., van Oost G., Gao F., Van Neck D. and Zhurkin E. E. 2014 *Journal of Physics: Condensed Matter* **26** 395001
- [70]Fukai Y. and Okuma N. 1994 *Phys. Rev. Lett.* **73** 1640
- [71]Fukai Y. 2003 *J. Alloys Compd.* **356-357** 263
- [72]Pathak S., Shaffer J. and Kalidindi S. R. 2009 *Scr. Mater.* **60** 439
- [73]Love A. 1939 *Q J Math* 161
- [74]Pathak S., Kalidindi S. R., Weaver J. S., Wang Y., Doerner R. P. and Mara N. A. 2017 *Sci. Rep.* **7**

- [75]Patel D. K. and Kalidindi S. R. 2016 *Acta Mater.* **112** 295
- [76]Kim J.-Y., Jang D. and Greer J. R. 2010 *Acta Mater.* **58** 2355
- [77]Yao W. Z., Wang P., Manhard A., Krill C. E. and You J. H. 2013 *Mater. Sci. Eng. A* **559** 467
- [78]Zayachuk Y., Armstrong D. E. J., Bystrov K., Van Boxel S., Morgan T. and Roberts S. G. 2017 *J. Nucl. Mater.* **486** 183
- [79]Fang X., Kreter A., Rasinski M., Kirchlechner C., Brinckmann S., Linsmeier C. and Dehm G. 2018 *J. Mater. Res.* **33** 3530
- [80]Nowak R., Pessa M., Sukanuma M., Leszczynski M., Grzegory I., Porowski S. and Yoshida F. 1999 *Appl. Phys. Lett.* **75** 2070
- [81]Schuh C. A., Mason J. K. and Lund A. C. 2005 *Nat Mater* **4** 617
- [82]Shim S., Bei H., George E. P. and Pharr G. M. 2008 *Scr. Mater.* **59** 1095
- [83]Morris J. R., Bei H., Pharr G. M. and George E. P. 2011 *Phys. Rev. Lett.* **106** 165502
- [84]Wang L., Bei H., Li T. L., Gao Y. F., George E. P. and Nieh T. G. 2011 *Scr. Mater.* **65** 179
- [85]Pathak S., Riesterer J. L., Kalidindi S. R. and Michler J. 2014 *Appl. Phys. Lett.* **105** 161913
- [86]Jin K., Xia Y., Crespillo M., Xue H., Zhang Y., Gao Y. F. and Bei H. 2018 *Scr. Mater.* **157** 49
- [87]Patel H. D. and Lee S.-W. 2020 *Scr. Mater.* **175** 16
- [88]Wang M. G. and Ngan A. H. W. 2004 *J. Mater. Res.* **19** 2478
- [89]Soer W. A., Aifantis K. E. and De Hosson J. T. M. 2005 *Acta Mater.* **53** 4665
- [90]Britton T. B., Randman D. and Wilkinson A. J. 2011 *J. Mater. Res.* **24** 607
- [91]Kato D., Iwakiri H. and Morishita K. 2011 *J. Nucl. Mater.* **417** 1115
- [92]Gao L., Jacob W., von Toussaint U., Manhard A., Balden M., Schmid K. and Schwarz-Selinger T. 2017 *Nucl. Fusion* **57** 016026
- [93]Zibrov M., Egger W., Heikinheimo J., Mayer M. and Tuomisto F. 2020 *J. Nucl. Mater.* 152017
- [94]Chen Y. Z., Ma X. Y., Shi X. H., Suo T., Borchers C., Zhang K. H., Liu F. and Kirchheim R. 2015 *Scr. Mater.* **98** 48
- [95]Fang X., Rasinski M., Kreter A., Kirchlechner C., Linsmeier C., Dehm G. and Brinckmann S. 2019 *Scr. Mater.* **162** 132
- [96]Sethna J. *Statistical mechanics: entropy, order parameters, and complexity*: Oxford University Press, 2006
- [97]Parrish W. 1960 *Acta Crystallogr.* **13** 838
- [98]Hull D. and Bacon D. J. *Introduction to dislocations*: Elsevier, 2011
- [99]Ma A. and Roters F. 2004 *Acta Mater.* **52** 3603
- [100]Pathak S., Stojakovic D., Doherty R. and Kalidindi S. R. 2009 *J. Mater. Res.* **24** 1142
- [101]Lorenz D., Zeckzer A., Hilpert U., Grau P., Johansen H. and Leipner H. S. 2003 *Phys. Rev. B* **67** 172101
- [102]Schuh C. A. and Lund A. C. 2004 *J. Mater. Res.* **19** 2152
- [103]Terentyev D., Bakaeva A., Pardoën T., Favache A. and Zhurkin E. E. 2016 *J. Nucl. Mater.* **476** 1
- [104]Li Y.. *et al* 2020 *Nucl. Fusion* **60** 046029